

Precipitation behavior in G-phase strengthened ferritic stainless steels

Mujin Yang ^{a, c}, Daniel J M King ^b, Ivan Postugar ^d, Yuren Wen ^e, Junhua Luan ^f, Bernd Kuhn ^g,
Zengbao Jiao ^h, Cuiping Wang ^{i, *}, M R Wenman ^b, Xingjun Liu ^{j, c, a, *}

^a School of Materials Science and Engineering, Harbin Institute of Technology, Shenzhen, Guangdong 518055 P.R. China

^b Department of Materials and Centre for Nuclear Engineering, Imperial College London, South Kensington, London, SW7 2AZ, United Kingdom

^c Institute of Materials Genome and Big Data, Harbin Institute of Technology, Shenzhen 518055, PR China

^d Central Institute for Engineering, Electronics and Analytics (ZEA-3) - Analytics, Forschungszentrum Jülich GmbH, 52425 Jülich, Germany

^e School of Materials Science and Engineering, University of Science and Technology Beijing, Beijing 100083, China

^f Department of Materials Science and Engineering, City University of Hong Kong, Hong Kong, China

^g Institute of Energy and Climate Research (IEK), Microstructure and Properties of Materials (IEK-2), Forschungszentrum Jülich GmbH, 52425 Jülich, Germany

^h Department of Mechanical Engineering, The Hong Kong Polytechnic University, Hong Kong, China

ⁱ College of Materials and Fujian Provincial Key Laboratory of Materials Genome, Xiamen University, Xiamen 361005, China

^j State Key Laboratory of Advanced Welding and Joining, Harbin Institute of Technology, Harbin 150001, PR China

*Corresponding author. E-mail: xjliu@hit.edu.cn; wangcp@xmu.edu.cn;

Tel: +86-592-2187888; Fax: +86-592-2187966

ABSTRACT

A series of G-phase strengthened ferritic stainless steels Fe-20Cr-3Ni-3Si-X (X=2Mn, 1Mn-2Ti, 1Mn-2Nb and 1Mn-2Ta) are characterized after aging using experimental (microhardness, TEM and APT) and theoretical (DFT) techniques. The results indicate that the Ni₁₆Mn₆Si₇ G-phase shows sluggish precipitation during aging treatment. This was attributed to the small difference in the enthalpy of formation between the Ni₁₆Mn₆Si₇ G- and BCC phase and the requirement of high Ni:Fe ratio. A superfine Ni₁₆Ti₆Si₇ G-phase was found to precipitate as a core accompanied with an “envelope” of Fe₂TiSi-L2₁ Heusler phase during early aging (≤24 h) in the Ti containing alloy. This morphology is predicted to occur due to early Ni clustering in

ferrite and a negative Ni concentration gradient away from the cluster that favors Fe₂TiSi formation. The G-phases show only particle coarsening without obvious chemical composition evolution for further aging up to 96 h. A prominent hardness increase of 100-275 HV was also observed during aging. These findings provide valuable insight into methods for precipitating low lattice mismatch silicide phases for the development of future high strength steels.

Keywords: Ferritic stainless steel; Aging hardening; Nano-precipitation; G-phase; Atom probe tomography;

1. Introduction

Stoichiometric G-phase exists as $A_{16}M_6Si_7$ ($Fm\bar{3}m$), where the A-site can be Fe, Co or Ni while transitional metals like Ti, Nb, Ta, Zr, Hf and Mn may occupy the M-site [1, 2]. This phase is most prevalent in aged austenitic and duplex stainless steels [3-9].

The discovery of the G-phase dates back to more than 60 years, when it was first reported by Beattie and Versnyder in 1956, in a precipitation-hardened austenitic stainless steel (A286) [10]. However, the exact conditions that led to its formation were not clear. Early studies observed the G-phase to form on residual grain boundaries and particles of NbC, between 500°C and 800°C in Nb-stabilised 20/25 austenitic steels [11-14]. It is now clear that G-phase forms in a series of austenitic steels with a general feature of forming predominantly on grain boundaries (hence the “G” phase designation). Furthermore, it was assumed to substantially deteriorate the mechanical properties of the materials.

In duplex stainless steels, G-phase was observed in the ferrite after prolonged service times at temperatures between 250 and 400°C [4, 6, 8, 15, 16]. As Mateo *et al.* [4] proposed, elemental Ni, Mn and Si may segregate to the α/α' interface before the structural transformation to G-phase occurs. With the help of atom probe tomography (APT), Pareige *et al.* [6] observed fine Ni-Mn-Si-rich particles at the α/α' interface, which supports the view of Mateo *et al.* Subsequently, the critical size and composition for the structural transformation of ferrite to G-phase were further revealed by Matsukawa *et al.* [8].

Up to now, there has been much research focused on inhibiting the precipitation of the G-phase, although the contribution of the G-phase to the deterioration of fracture toughness of duplex stainless is still a matter of controversy. Conversely, the concept of promoting the G-phase precipitation as a strengthening phase is relatively unexplored. Work on the latter subject began in 1989 with Schulz-Beeken and Hougardy (S.H.) who were the first to deliberately precipitate the G-phase for strengthening. A high tensile yield strength of ~1.8 GPa was achieved in their newly developed low-alloy maraging

steel [17]. Subsequently, the G-phase was found to contribute to significant aging-hardening in a Co-free and Cr-containing maraging steel [18, 19]. Very recently, Sun *et al.* [20] characterized the previous S.H. alloy and several other G-phase strengthened Fe-based martensitic alloys by APT and in-situ small angle X-ray scattering (SAXS), revealing the highest G-phase number-density ($\sim 10^{25} \text{ m}^{-3}$) of structural materials discovered so far, and the maximum compressive yield strength was measured to be 2.0 GPa. All the above mentioned studies revealed that the G-phase forms as spherical precipitates with a cube-on-cube coherent orientation to the surrounding martensitic matrix.

One of the benefits of the G-phase strengthening is the potential for conserving the ductility of the alloy due to its coherency with the ferritic matrix. Recently, it has been theorized that it may be possible to fine-tune this coherency through altering the chemical composition of the G-phase [21]. This concept presents a significant number of G-phase compositions that could potentially be exploited in advanced Fe-base alloys. Seventeen different G-phase chemistries have been theoretically investigated in our previous studies, and preliminary investigations of four different G-phase precipitating alloys ($\text{Ni}_{16}\text{Zr}_6\text{Si}_7$, $\text{Ni}_{16}\text{Ti}_6\text{Si}_7$, $\text{Ni}_{16}\text{Nb}_6\text{Si}_7$ and $\text{Ni}_{16}\text{Ta}_6\text{Si}_7$) have been investigated experimentally [21-24].

In this study, the G-phase precipitation behaviors of $\text{Ni}_{16}\text{Mn}_6\text{Si}_7$, $\text{Ni}_{16}\text{Ti}_6\text{Si}_7$, $\text{Ni}_{16}\text{Nb}_6\text{Si}_7$ and $\text{Ni}_{16}\text{Ta}_6\text{Si}_7$ have been comprehensively investigated during the isothermal-aging of a series of typical G-phase reinforced stainless steels Fe-20Cr-3Ni-3Si-X (X=2Mn, 1Mn-2Ti, 1Mn-2Nb and 1Mn-2Ta). Electron microscopy and atom probe tomography (APT) characterization together with density functional theory (DFT) studies have been performed to understand the microstructural evolution (particle size, volume fraction, number-density and chemistry) of the typical Fe-20Cr-based ferritic steels, which is beneficial to the further development of this new steel family.

2. Methodology

2.1 Experimental

A series of Fe-20Cr-3Ni-3Si-X (X=2Mn, 1Mn-2Ti, 1Mn-2Nb and 1Mn-2Ta) ferritic alloys were arc-melted in an Ar atmosphere cast in a copper-mold. For simplicity, these alloys are further referred to as 2Mn, 2Ti, 2Nb and 2Ta. The corresponding nominal chemical compositions of each alloy are shown in Table 1. The ingots of $\sim 0.03 \times 0.01 \times 0.08$ m dimensions were homogenized at 1300°C for 0.5 h and then cold rolled with a $\sim 60\%$ thickness reduction. Subsequently, samples were cut from the cold-rolled plates, solution treated at 1300°C for 0.25 h and aged at 560°C for 0, 24, 48 and 96 h. Additional samples for long term aging were cut from the 2Mn alloy and aged at 400, 500, 600 and 700°C for up to 90 days.

Table 1. The nominal compositions of alloys in this work (wt.%)

Label	Cr	Ni	Si	Mn	Ti	Nb	Ta	Fe
2Mn	20	3	3	2	/	/	/	Bal. Fe
2Ti	20	3	3	1	2	/	/	Bal. Fe
2Nb	20	3	3	1	/	2	/	Bal. Fe
2Ta	20	3	3	1	/	/	2	Bal. Fe

Micro-hardness tests were carried out on the aged specimens with a load of 9.8 N and a hold time of 10 s. The averaged values of seven points are reported. Some of the aged specimens were further analyzed using scanning electron microscopy (SEM), transmission electron microscopy (TEM) and APT. SEM specimens were cut from aged samples, cold mounted with epoxy resin and polished to a sub-micron finish applying a suspended diamond polishing solution. The microstructure was examined by high-resolution field emission scanning electron microscopy (backscatter electron imaging). For TEM analyses, slices ~ 1 mm thick were cut from aged samples, ground to a thickness of ~ 50 μm and were then electro-polished at room temperature. They were then jet-polished using 28 V in an electrolyte containing 6% HClO₄, 12% CH₃COOH and 12% ethylene glycol in methanol. Thin foils were examined in a JEM-2100 (HC) TEM operating at 200 kV. The images were analysed using the “Image J” software.

Needle-shaped APT specimens were fabricated by annular milling in a FEI Scios or FEI Helios 600i dual beam focused ion beam (FIB) tools following a conventional lift-out method [25]. APT characterizations were performed using local electrode atom probes LEAP 4000X HR and 5000XR (Cameca instruments). The specimens were analysed in voltage mode (pulse repetition rate 200 kHz and pulse fraction 0.2) as well as in laser mode (pulse repetition rate 250 kHz and pulse energy 50 pJ). The specimen base temperature was maintained at 50 K and the ion collection rate was 0.5% or 1% per pulse. Interactive Visualization and Analysis Software (IVAS™, Versions 3.6.14 and 3.8) was utilized for building three-dimensional reconstructions and data analyses. More details on APT data processing can be found in the Supplementary materials.

2.2 Theoretical

A plane-wave DFT method was used, implemented in the Vienna Ab initio Simulation Package (VASP) [26]. Projector augmented wave (PAW) pseudopotentials [27] were used for each element. Semi-core p states were considered valence electrons for Fe (14), Mn (13), Nb (11) Ni (16), Ta (11), Ti (10), V (11), and a standard number of electrons Si (4). The k-points, cut-off energy and lattice parameters of the pure elements in their ground state structures were converged independently. A real space k-point density of 0.02 \AA^{-3} and a cut-off energy of 500 eV would provide accurate results, within 10^{-3} eV, and were kept consistent to calculate formation enthalpies and lattice parameters in all alloyed structures. The Methfessel and Paxton [28] smearing method (width 0.1 eV) was used and full geometry relaxations were carried out under constant pressure for all reference structures. Spin polarization effects were included. For the exchange-correlation functional, the generalized gradient approximation as developed by Perdew *et al.* [29] (GGA-PBE) was utilized. The convergence criterion for electronic convergence was 10^{-6} eV and for geometry optimization was 10^{-4} eV. The formation enthalpies of the disordered structures were computed using the same methodology as previously performed on these systems [21, 30]. For the $(\text{Ni}_x\text{Fe}_{1-x})_{16}\text{M}_6\text{Si}_7$ G-phase/BCC and $(\text{Ni}_x\text{Fe}_{1-x})_2\text{MSi}$ L₂₁ structures, the formation enthalpies were interpolated between

end members except in the case for $M = \text{Mn}$ in the G-phase where enthalpies were taken from previously published calculations [31].

3. Results

3.1 Aging response

Figure 1 displays microhardness results for the 2Mn, 2Ti, 2Nb and 2Ta alloys at different initial states, aging temperatures and times. The 2Mn alloy negligibly changes in hardness (250 ± 10 HV) throughout the aging process at 500°C, from several hours to 90 days, which implies a long incubation period (>90 days) is needed for $\text{Ni}_{16}\text{Mn}_6\text{Si}_7$ G-phase precipitation in a fully ferritic stainless steel. In the past, Ni-Mn-Si precipitates have been reported to be “late blooming” in low-alloyed ferritic steels [32, 33]. In **Figure 1a** the inserted TEM micrograph and diffraction pattern are taken from the 500°C/90 days-aged 2Mn specimen, which clearly show a single ferritic microstructure with a few dislocations, which suggests that the late appearance of the Ni-Mn-Si precipitates in low-alloyed steels may also apply to the $\text{Ni}_{16}\text{Mn}_6\text{Si}_7$ G-phase in 20Cr ferritic stainless steels.

For promoting precipitation (i.e. shortening the incubation period), a cold rolling and subsequent aging strategy (referred to as CRA) was applied to the 2Mn alloy. The total thickness reduction was controlled to be ~60%. Effects of the aging-temperature on its micro-hardness response were plotted in **Figure 1b**. For isothermal aging at 400°C, 500°C, 600°C to 700°C (**Figure 1b**), the aging time was 90 days and thus can be compared directly to the maximum aged solution treated samples. **Figure 1b** shows the micro-hardness is significantly larger (~1.7×) in the cold rolled samples after aging at 400°C and 500°C compared to solution treated samples, implying that precipitation of the $\text{Ni}_{16}\text{Mn}_6\text{Si}_7$ G-phase had taken place in the CRA state. Further confirmation of this precipitation is provided in **Supplementary Figure S1**. The micro-hardness after aging at 600°C and 700°C is similar to that of the solution-treated state (~250 HV). Thus, we assume that the CRA strategy for the 2Mn alloy leads to the precipitation of the $\text{Ni}_{16}\text{Mn}_6\text{Si}_7$ G-phase for aging temperatures of 400°C and 500°C, but that the $\text{Ni}_{16}\text{Mn}_6\text{Si}_7$ G-phase is not thermodynamically stable at temperatures $\geq 600^\circ\text{C}$ [8, 34, 35].

Figure 1c shows that the micro-hardness does not increase from its pre-aged condition (~ 300 HV) until 90 days for the CRA sample, and shows no real increase in hardness for the sample that was not cold rolled. It is possible that the initial precipitation of $\text{Ni}_{16}\text{Mn}_6\text{Si}_7$ G-phase occurs sometime between 60 and 90 days. Even so, this incubation time is considered too long for practical steel manufacturing purposes.

Figure 1d presents re-plotted data from our previous work on 2Ti, 2Nb and 2Ta alloys [22] for ease of comparison. In contrast to the 2Mn alloy, the 2Ti, 2Nb and 2Ta alloys showed a much faster aging-hardening response. No incubation period >1 day was needed when aging at 560°C . Furthermore, the microstructure seems to be relatively stable, i.e. the hardness remains constant up to 96 h aging in 2Nb and 2Ta alloys and only a small decrease is observed in the 2Ti sample. To get more insights into the microstructure, the 400°C -, 500°C - and 560°C -aged specimens were carefully examined by TEM and APT and described in the following sections.

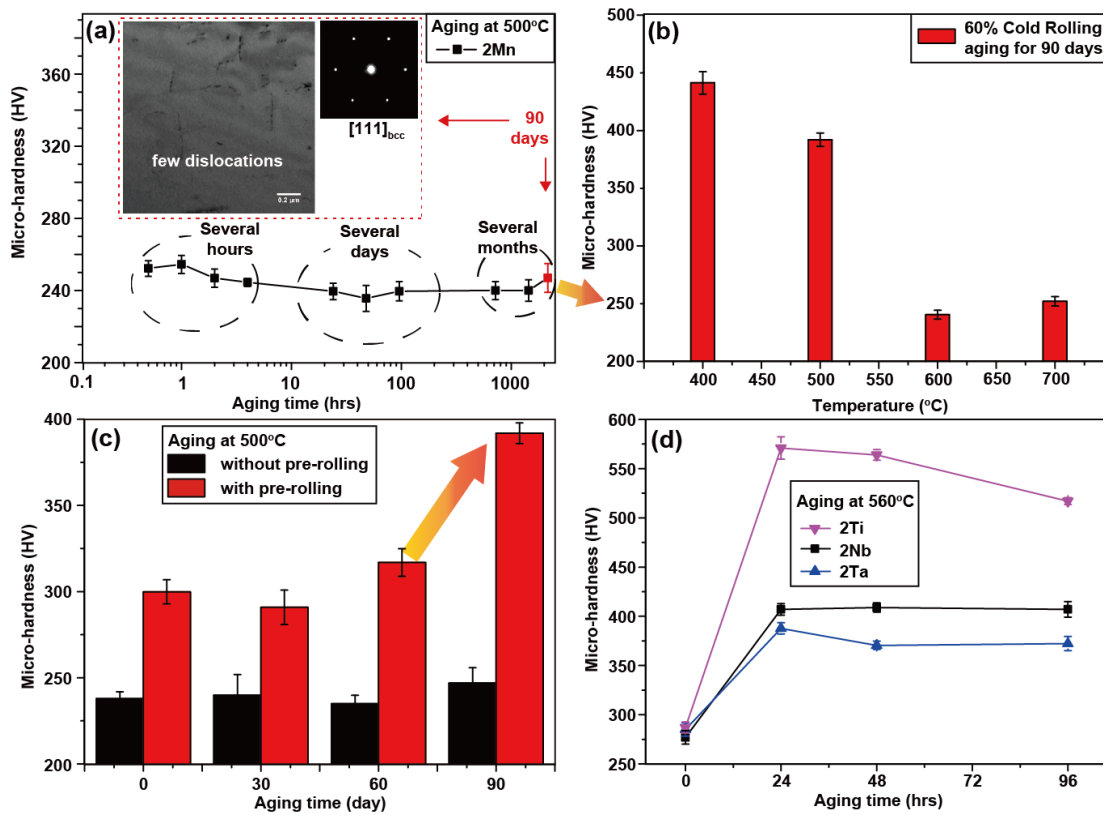


Figure 1. The micro-hardness as a function of (a) aging time for 2Mn at 500°C , (b) aging temperature for the pre-rolled 2Mn for 90 days, and (c) aging time for the pre-rolled 2Mn at 500°C ; (d) aging time for 2Ti, 2Nb and 2Ta alloy at 560°C . The inset

TEM micrograph and diffraction pattern in **Figure 1a** were taken from the 500°C/90 days aged 2Mn sample.

3.2 Microstructural characterization

3.2.1 The Ni₁₆Mn₆Si₇ G-phase

Figure 2 displays the microstructural characteristics of the cold rolling and subsequent aging (CRA) treated 2Mn specimens. **Figure 2a, b, c** and **d** were produced from the 400°C-CRA specimen, while the others (**Figure 2e to k**) were produced from the 500°C-CRA treated one. Low magnification back-scattering electron (BSE) images in **Figures 2a** and **e** show a lot of criss-crossed slip zones with a spacing of ~100 μm. No recrystallized grains were found, which means the recrystallization temperature of the 2Mn alloy is higher than 500°C. Both **Figure 2b** and **f** show a typical double-electron-diffraction pattern, which strongly implies there are precipitates in the ferrite grain interiors. Diffraction pattern indexing is indicative of a body-centered-cube (BCC) matrix and face-centered-cubic (FCC) precipitate. The matrix and precipitate obey a strict cube-on-cube orientation relationship ($[110]_F//[110]_p$, $[100]_F//[100]_p$, $(002)_F//(008)_p$, $(-110)_F//(-440)_p$, $(020)_F//(080)_p$), which is further illustrated by the lattice parameter of the precipitate being ~4 times that of the ferritic matrix. This is typical of G-phase precipitates in a ferrite matrix [8, 15]. The bright field (BF) images in **Figure 2c** and **g**, and its corresponding dark field (DF) images in **Figure 2d** and **h** together reveal the nanoscale morphologies of the Ni₁₆Mn₆Si₇ G-phase in the samples aged at 400°C and 500°C for 90 days. The G-phase appears as a spherical superfine particle with a diameter <10 nm (**Figure 2d**) when aged at 400°C for 90 days. However, the precipitates become more cuboidal with a side-length of 40-50 nm (**Figure 2h**) when aged at 500°C for 90 days. Using several DF images (>80 particles), the averaged phase fraction for Ni₁₆Mn₆Si₇ G-phase at 500°C was estimated to be ~2.3 % (area fraction).

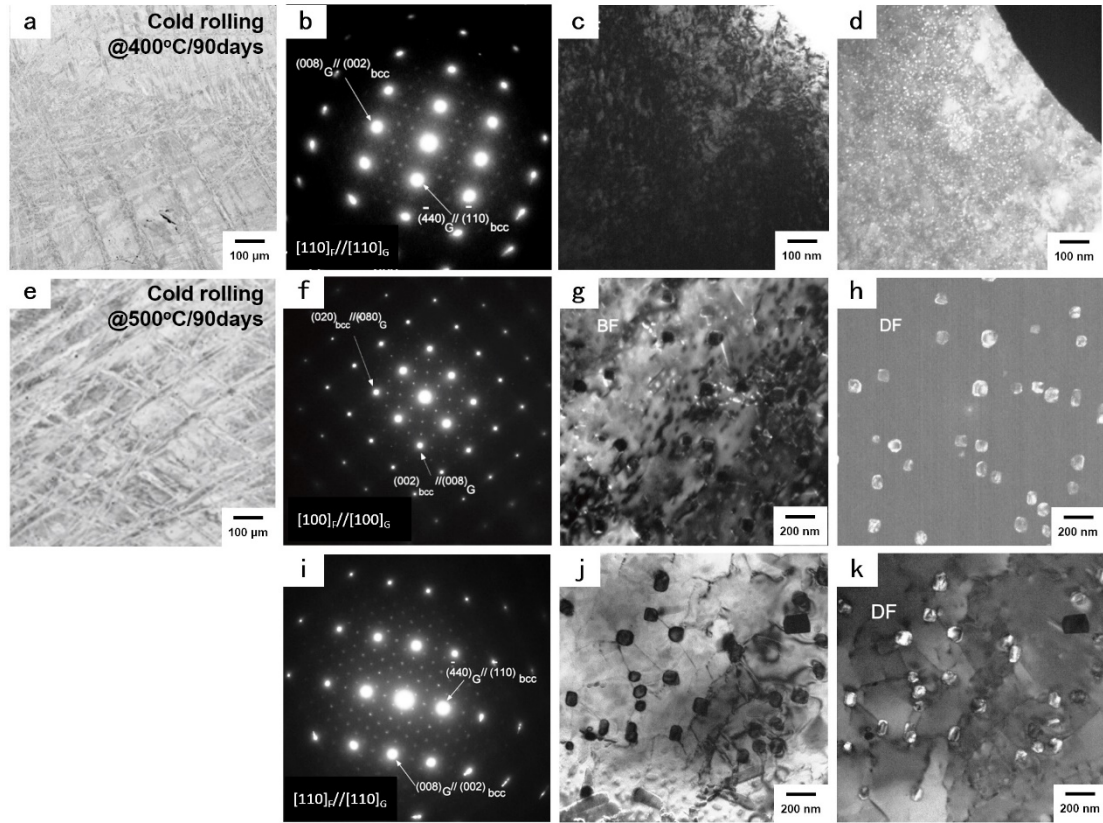


Figure 2. Microstructural observation of the 2Mn alloy after cold-rolling and subsequent 90 days-aging treatment: (a) and (e) are back-scattered-electron (BSE) images; (b), (f) and (i) are selected area electron diffraction (SAED) from the 110_F , 100_F and 110_F incident, respectively; (c), (g) and (j) are bright field (BF) images; (d), (h) and (k) are dark field (DF) images taken from the -220_G spot in **Figure 2b**, the 040_G in **Figure 2f** and the -220_G in **Figure 2i**, respectively. (**Figure 2a** to **2d** was taken from the 400°C -aged specimen and **Figure 2e** to **2k** was taken from the 500°C -aged specimen).

To elucidate the role of cold-rolling on promoting the $\text{Ni}_{16}\text{Mn}_6\text{Si}_7$ G-phase precipitation, the 500°C -CRA treated 2Mn specimen was further analyzed in the 110_F crystal zone axis as shown in **Figure 2i**. The BF (**Figure 2j**) and the corresponding DF images (**Figure 2k**) co-display that the precipitation site of these coarsened G-phase particles occurred at the intersection of dislocation lines. Thus, it can be inferred that the dislocation intersections induced by cold-rolling provide nucleation sites, and thus reduce the nucleation barrier for the precipitation of the $\text{Ni}_{16}\text{Mn}_6\text{Si}_7$ G-phase in the ferritic matrix.

3.2.2 The $\text{Ni}_{16}\text{Ti}_6\text{Si}_7$ G-phase and anomalous L_{21} phase

Figure 3 presents the results of APT characterization from the 560°C/24h-aged 2Ti alloy. The 20 nm thick slice from the reconstructed atom maps for Fe, Cr, Si, Mn, Ni and Ti is shown in **Figure 3a**, illustrating the precipitates are enriched in Ni, Ti and Si with a strong rejection of Fe, Cr and Mn. The isosurfaces of the 10 at.% Ti and 10 at.% Ni are shown together in **Figure 3b**, depicting that positions of Ti- (purple) and Ni-rich (green) precipitates overlap partially but do not coincide, indicating the presence of two types of precipitates. Local enlarged isosurfaces of the 10 at.% Ni in **Figure 3c** clearly show that Ti-rich regions partially extend outside Ni-rich cores, however, they do not constitute a complete core-shell structure. The isosurface of $C_{Ti}/C_{Ni}=2$ better depicts the arrangement that we term an “envelope” where the inner Ni-rich precipitates protrude from the Ti-rich shell into the matrix. The corresponding concentration profiles across the interfaces of Ni-rich precipitates and Ti-rich envelopes (built as proximity histograms) are shown in **Figure 3d** and **e**, respectively. It should be noted that the Ni-rich phase also contains ~10 at.% Fe, and Ti-rich envelope contains as little as ~3 at.% Ni, and almost no Cr and Mn were observed inside them. The chemical compositions in the precipitate cores are summarized in **Supplementary Table S1**. The results indicate that the Ni-rich phase should be a non-stoichiometric G-phase $(Fe,Ni)_{16}Ti_6Si_7$ while the composition of Ti-rich envelope corresponds to the $(Fe,Ni)_2TiSi$ phase ($L2_1$ structure).

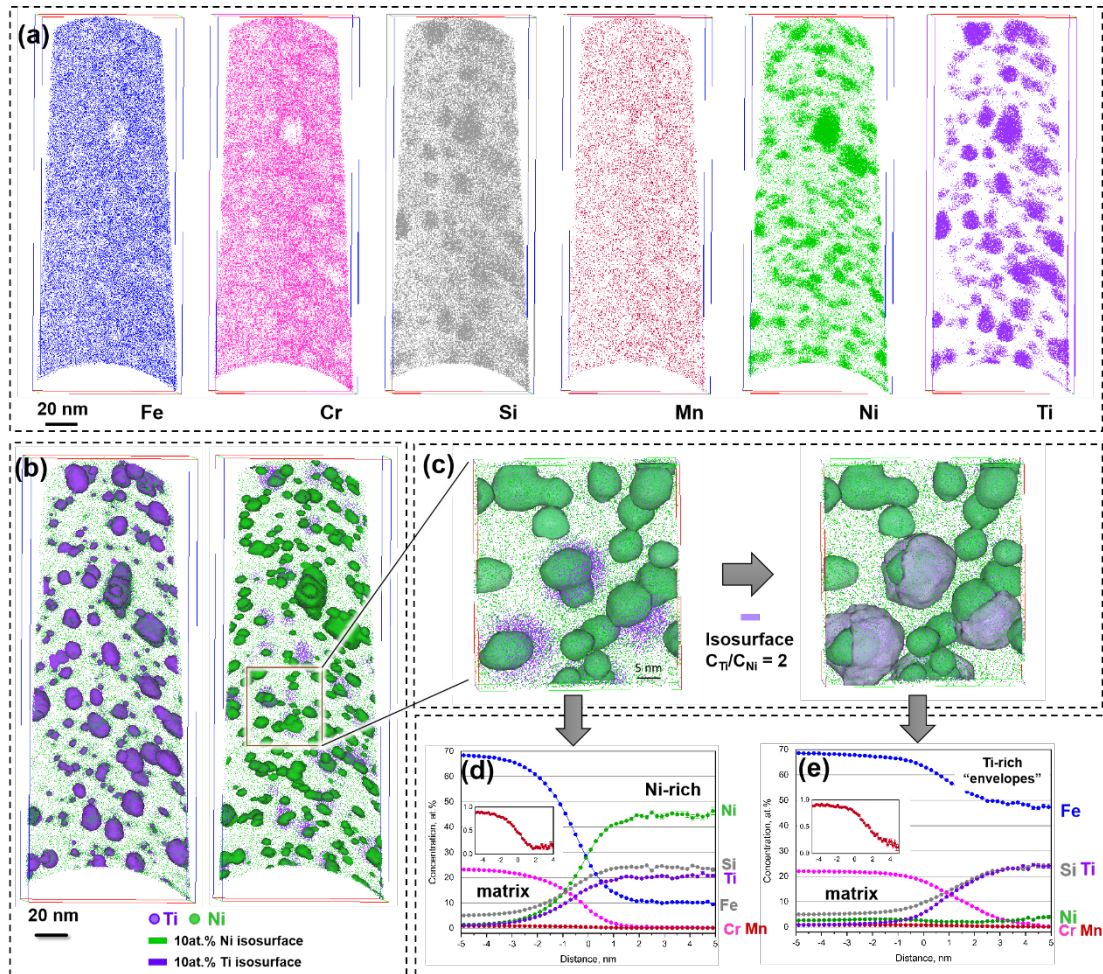


Figure 3. Atom probe analysis of the 560°C/24 h-aged 2Ti specimen: (a) 20 nm thick slice from atom maps for Fe, Cr, Si, Mn, Ni and Ti; (b) atom maps with isosurfaces of the 10 at.% Ti and 10 at.% Ni; (c) enlarged image from (b) with a corresponding isosurface of the $C_{Ti}/C_{Ni}=2$; (d) the composition profiles from the matrix to the Ni-rich phase; (e) the composition profiles from the matrix to the Ti-rich “envelope” phase.

Figure 4 shows two high-resolution TEM images and the corresponding fast Fourier transform (FFT), which was taken from the 560°C/24h-aged 2Ti alloy. The semi-closed (**Figure 4a**) and fully closed (**Figure 4d**) envelope structures with a diameter of 8~10 nm were clearly imaged from the perspective of the 110_F incident directions. These two envelope morphologies are consistent with those observed in the APT analyses since TEM shows a 2D projection, while the “opening” may be in the direction perpendicular to the image plane. The indexing of FFT patterns (**Figure 4b, c, e and f**) from different regions indicated the envelope regions (G and $L2_1$ in **Figure 4a** and **e**) belong to G-phase and ordered $L2_1$ phase, respectively. And the ferritic matrix, G-phase and $L2_1$ maintains a cube-on-cube orientation relationship: $110_F//110_G//110_{L2_1}$,

$100_{\text{F}}//100_{\text{G}}//100_{\text{L2}_1}$, $(008)_{\text{G}}//(004)_{\text{L2}_1} //(002)_{\text{A2}}$, $(080)_{\text{G}}//(040)_{\text{L2}_1} //(020)_{\text{A2}}$,
 $(222)_{\text{G}} //(111)_{\text{L2}_1}$.

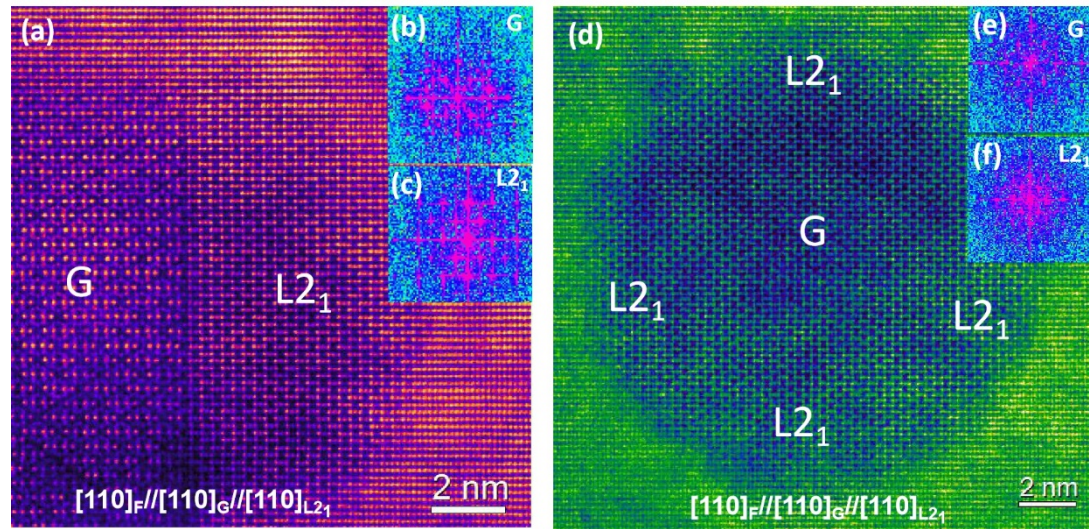


Figure 4. The TEM analysis of the 560°C/24 h-aged 2Ti films: the high-resolution transmission electron images (a) and (d); the fast Fourier transform (FFT) images (b), (c), (e) and (f). (the subscript “F” refers to ferritic matrix).

The APT characterization of the 560°C/96h-aged 2Ti alloy is shown in **Figure 5** to examine microstructural evolution during isothermal aging. The precipitates are enriched in Ni, Ti and Si according to the atom maps in **Figure 5a**, and it can be inferred that the precipitate morphology does not change significantly from the 24 h aged condition (G and L2₁ in **Figure 3a**). The C_{Ti}/C_{Ni}=2 isosurface (**Figure 5b**) clearly depicts the hierarchical microstructure of precipitates, which consist of single G-phase as well as G-core/L2₁-envelope structures.

The configuration of precipitates after 560°C/96h is qualitatively similar to that after 560°C/24h aging. Each L2₁-precipitate contains a G-phase precipitate as a core, so the G-phase apparently serves as a nucleation site for L2₁ phase; stand-alone L2₁ precipitates were found neither in 560°C/24h nor in 560°C/96h samples. **Figure 5c** and **d** present the concentration profiles from the matrix to the G and L2₁ phases, respectively, which show the same precipitate compositions as in the 560°C/24h-aged sample. Thus, it is proposed that aging for 24 h is sufficient for reaching the equilibrium compositions by diffusion.

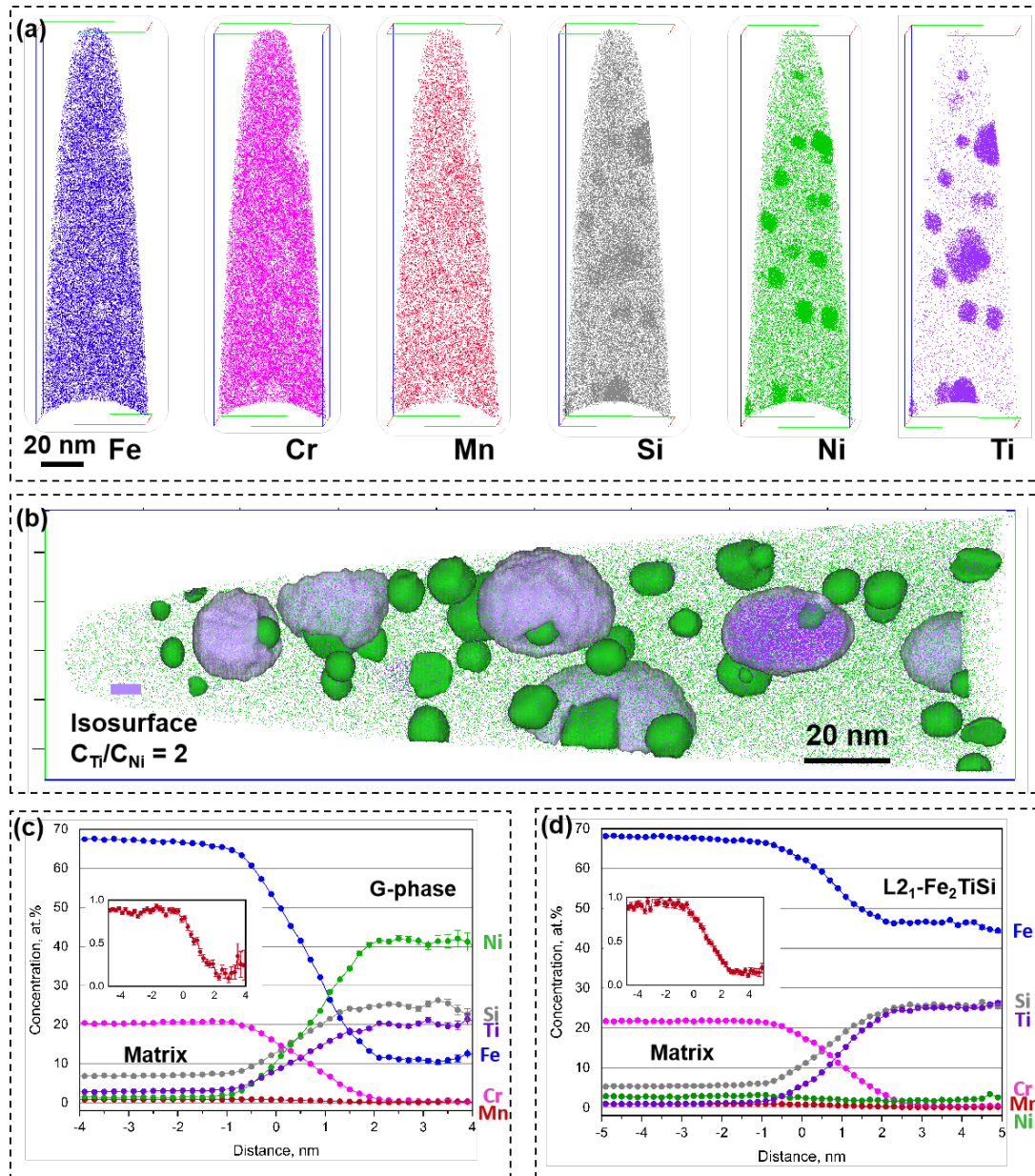


Figure 5. Atom probe analysis of the 560°C/96 h-aged 2Ti alloy: (a) 20 nm thick slice from atom maps for Fe, Cr, Si, Mn, Ni and Ti; (b) precipitate visualization with the 10 at.% Ni (green, G-phase) and $C_{Ti}/C_{Ni}=2$ (violet, L2₁ phase) isosurfaces; (c) the composition profiles from the matrix to the G-phase; (e) the composition profiles from the matrix to the L2₁ phase.

3.2.3 The Ni₁₆Nb₆Si₇ G-phase

Atom probe analyses of the 2Nb alloy aged at 560°C for 24 h and 96 h are presented in **Figure 6**. The 20 nm thick slices from atom maps for Fe, Cr, Si, Mn, Ni and Nb for both the 24 h-aging (**Figure 6a**) and the 96 h-aging (**Figure 6b**) illustrated that precipitates are enriched in Ni, Nb and Si. **Figure 6c** and **f** depict the corresponding

isosurfaces of the 3 at.% Nb, indicating only one type of precipitate form in this alloy. It should be noted that precipitate sizes in APT maps may be slightly overestimated and elongated due to the local magnification effect (APT artifact). The composition profiles from matrix to G-phase for 24 h- and 96 h-aging are displayed in **Figure 6d** and **e**, respectively. Note that G-phase contains a higher Fe concentration (~30 at. %) than Ni (~26 at. %) and a notable amount of Cr (~4 at. %) at the expense of both Si and Nb. Thus, we deduced that Fe and Ni form a G-phase base together (i.e. $(\text{Fe, Ni})_{16}\text{Nb}_6\text{Si}_7$ phase). It is clear that the $(\text{Fe, Ni})_{16}\text{Nb}_6\text{Si}_7$ G-phase precipitates grow with an increasing aging-time while their composition remains constant.

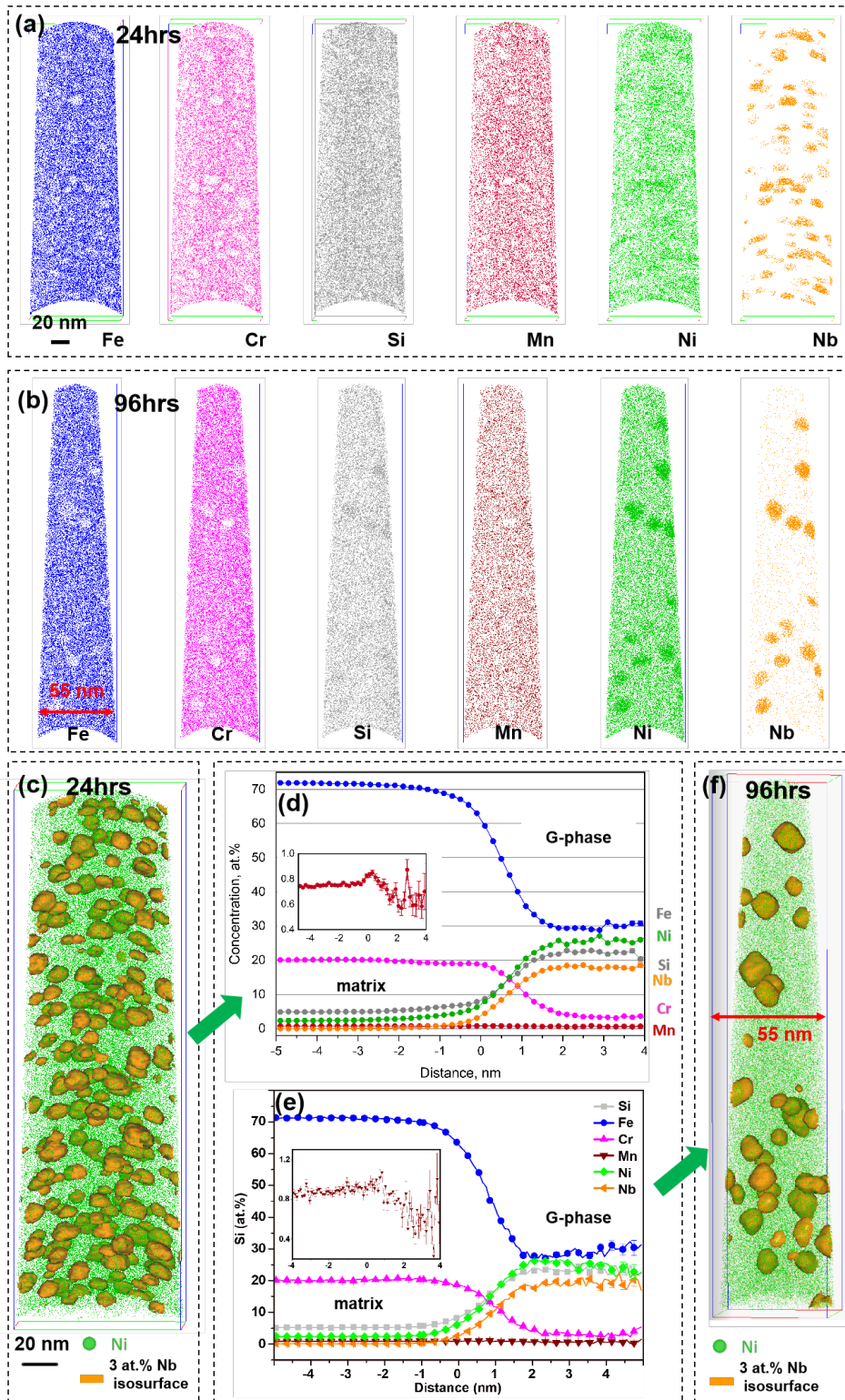


Figure 6. APT analysis of the 2Nb alloy: (a) 20 nm thick slice from atom maps for Fe, Cr, Si, Mn, Ni and Nb for 24 h-aging; (b) atom maps for Fe, Cr, Si, Mn, Ni and Nb for 96 h-aging; (c) precipitate visualization with the 3 at.% Nb isosurfaces for 24 h-aging; (d) the composition profiles from the matrix to the G-phase for 24 h-aging; (e) the composition profiles from the matrix to the G-phase for 96 h-aging; (e) precipitate

visualization with the 3 at.% Nb isosurfaces for 96 h-aging.

3.2.4 The $\text{Ni}_{16}\text{Ta}_6\text{Si}_7$ G-phase

Figure 7 shows the precipitation of $\text{Ni}_{16}\text{Ta}_6\text{Si}_7$ G-phase in the 24h- and 96h-aged specimens is very similar to the case of the $\text{Ni}_{16}\text{Nb}_6\text{Si}_7$ G-phase. The precipitates are enriched in Ni and Ta but depleted of Fe, Cr and Mn, as shown in **Figure 7a** and **b**. The comparison of isosurfaces of 5 at.% Ta (**Figure 7c** and **d**) again show particle coarsening over time. Furthermore, the $\text{Ni}_{16}\text{Ta}_6\text{Si}_7$ G-phase showed a high concentration of Fe (~30 at.%) similar to that in $\text{Ni}_{16}\text{Nb}_6\text{Si}_7$. In the following section, the particle size, volume fractions, coarsening behavior, and aging responses of the three compositions, $\text{Ni}_{16}\text{M}_6\text{Si}_7$ G-phases (M=Ti, Nb, Ta), are compared and discussed.

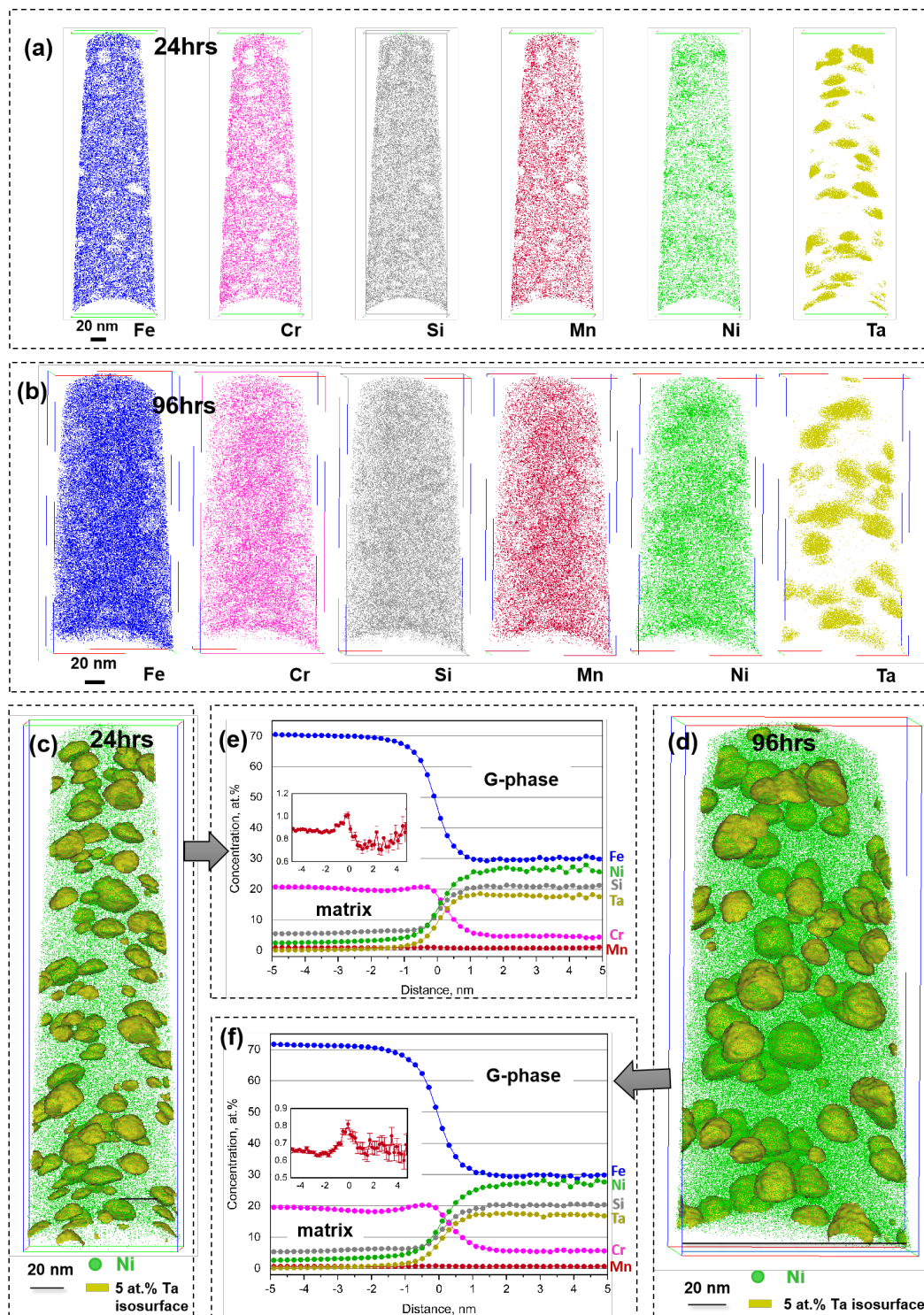


Figure 7. Atom probe analysis of the 2Ta alloy: (a) 20 nm thick slice from atom maps for Fe, Cr, Si, Mn, Ni and Ta for 24 h-aging; (b) atom maps for Fe, Cr, Si, Mn, Ni and Ta for 96 h-aging; (c) precipitate visualization with the 5 at.% Ta isosurface for 24 h-aging; (d) precipitate visualization with the 5 at.% Ta isosurface for 96 h-aging; (e) the composition profiles from the matrix to the G-phase for 24 h-aging; (f) the composition profiles from the matrix to the G-phase for 96 h-aging.

3.3 Precipitate chemistry (DFT calculations)

Three structures were modeled using calculations based on DFT: BCC, L2₁ and G-phase, see **Figure 8**. The chemistry of these structures were (Ni_xFe_{x-1})₁₆M₆Si₇, for the BCC and G-phase structures, and (Ni_xFe_{x-1})₂M₂Si for the L2₁ structure, where M = Mn, Nb, Ta, and Ti and x was varied from 0 to 1. The lattice parameters (a), formation enthalpies (H_f) and magnetic moments of each L2₁ structure/chemistry are reported in **Table 2**. These lattice parameters are roughly double that of the simulated pure BCC Fe lattice parameter (2.83 Å) [36]. It is plausible that such precipitates could have a coherent interface with the surrounding ferrite matrix and the G-phase. However, the thermodynamic drive force for their formation is dependent on their enthalpies of formation, relative to other possible phases.

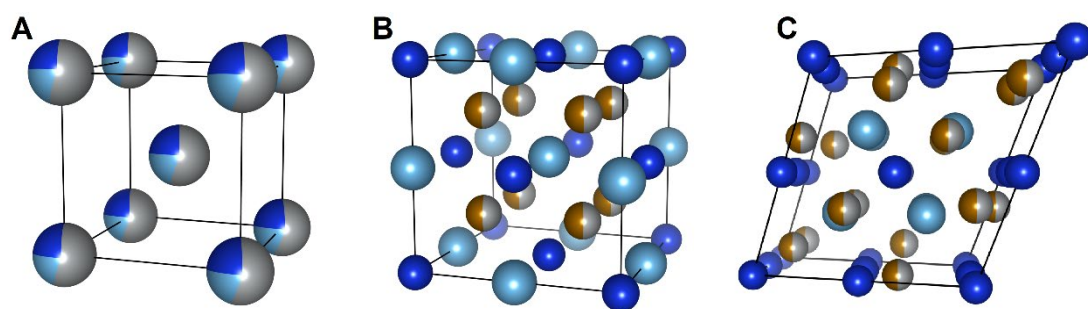


Figure 8. Atomic structures of (A) BCC, (B) L2₁ and (C) G-phase where Fe, M, Ni and Si are colored bronze, light blue, silver and dark blue, respectively, and M = Mn, Nb, Ta, and Ti.

Table 2. Lattice parameter (a), formation enthalpy (H_f) and magnetic moment of L2₁ structures of (Fe,Ni)₂MSi composition, where M = Nb, Mn, Ta and Ti.

L2 ₁ composition	a (Å)	H_f (kJ/mol)	Magnetic moment (μ_B)	
			Ni/Fe	M
Ni ₂ TiSi	5.79	-0.62	-	-
Ni ₂ MnSi	5.69	-0.36	0.26	3.34
Ni ₂ MnSi	5.61	-0.10	-	-
Ni ₂ NbSi	5.91	-0.33	-	-
Ni ₂ TaSi	5.90	-0.34	-	-
Fe ₂ TiSi	5.70	-0.69	-	-
Fe ₂ MnSi	5.58	-0.33	0.23	2.55
Fe ₂ MnSi	5.54	-0.12	-	-
Fe ₂ NbSi	5.85	-0.35	0.60	-0.17
Fe ₂ TaSi	5.84	-0.41	0.62	-0.14

Figure 9 compares the enthalpies of formation (H_f) for the three (Ni,Fe)-M-Si structures when x is varied from 0 to 1 (atomic fraction). The relative favorability of each structure when M = Mn is predicted to change from L2₁>BCC>G-phase with increasing Ni content. When M = Nb and Ta, the mixtures are predicted to form a G-phase compound for all Ni/Fe contents. In the M = Ti compositions, the L2₁ structure is predicted to be stable for the Fe rich compositions, this shifts to the G-phase for Ni rich compositions. It should be mentioned that the concentration, at which the change in favorability occurs, will be affected by temperature and off-stoichiometric enthalpies, which are not calculated here. Therefore, these results are more of a qualitative reference to infer the precipitate behavior.

The L2₁ (Ni,Fe)₂MnSi Heusler phase has been observed, in the past, to undergo a magnetic transition from a ferromagnetic to paramagnetic state at ($\sim 0^\circ\text{C}$) [37] for this reason the non-magnetic phase is used for comparison to the BCC and G-phase structures. It is predicted that the L2₁ phase could form in preference to BCC and G-phase for compositions with high Fe:Ni ratio in the (Ni,Fe)₂MnSi stoichiometry.

However, the $L2_1$ structure is not observed in the 2Mn aged samples examined in this study. This discrepancy could be explained by the assumption that Ni preferentially clusters in the ferrite [38-40] (followed by Mn and Si) and the Fe_2MnSi stoichiometry may not be achieved during aging. The long aging times required to precipitate the $Ni_{16}Mn_6Si_7$ G-phase may arise due to the small difference in its magnitude of enthalpy of formation to the BCC phase and the requirement of a high Ni:Fe ratio before the G-phase becomes the most favorable phase.

The G-phase structures containing Nb and Ta are predicted to be the most stable for all Fe:Ni ratios. Furthermore, the G-phase formation enthalpy is significantly lower than the BCC formation enthalpy. This supports the experimental observations of expedient precipitation and the high concentration of Fe in the G-phase observed in this study.

For the Ti containing compositions there is a strong preference for a non-magnetic $L2_1$ phase to form. If it is assumed that Ni clustering precedes Ti and Si then it is not surprising that the G-phase forms initially due to the Ni rich cluster composition. However, the G-phase may then transform to $L2_1$, or the $L2_1$ phase may simply nucleate at the G-phase/BCC interface due to the negative concentration gradient of Ni away from the center of the cluster/precipitate [41]. This is supported by the G/ $L2_1$ -envelope morphology observed experimentally in this study.

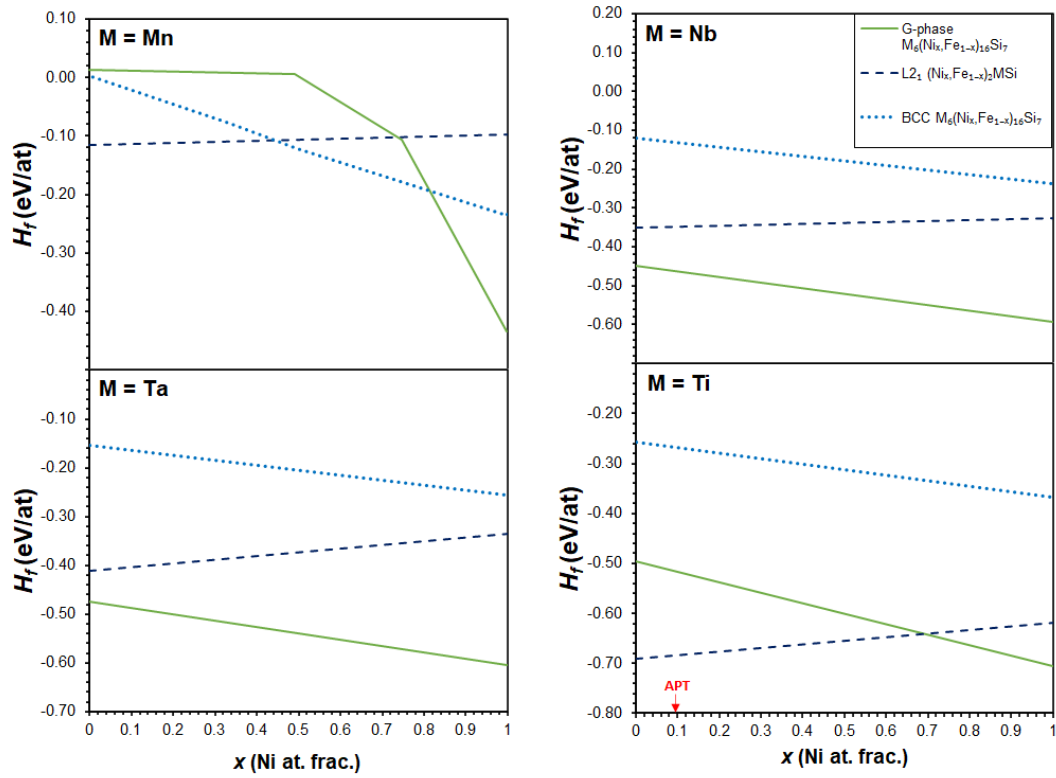


Figure 9. Formation enthalpies of BCC, G-phase and $L2_1$ structures with Ni atomic fractions from 0 to 1 and M species labeled in each panel where negative values are more favorable. The APT measured Ni content is marked with the red labeled arrow.

The DFT calculations performed here provide fundamental insight into the thermodynamic drive for precipitation within the alloys studied. Although a range of Ni/Fe chemistries are examined, comparisons should only be made between structures of the same chemistry to conserve mass. The difference in formation energies between the BCC and G-phase for compositions containing Nb, Ta and Ti is calculated to be ~ 0.30 eV/at for all Ni concentrations. However, for the Mn containing composition this difference is ~ 0.10 eV/at, for Ni concentrations that the G-phase is more energetically favorable (>0.8 at. frac.), which may be contributing factor towards the long aging times required before precipitation of the $Ni_{16}Mn_6Si_7$ G-phase in the 2Mn alloy observed in the current experiment. The anomalous $(Ni,Fe)_2TiSi$ $L2_1$ structure observed in the 2Ti alloy is predicted to be energetically stable for compositions richer in Fe. All G-phase and $L2_1$ chemistries observed experimentally, within the current study, are in agreement

with the lowest energy equilibrium structures. Although there is a trend in enthalpy for complete Ni enrichment (Fe depletion), not seen to occur with increasing age time experimentally, it is possible ulterior factors such as entropy, surface energy, kinetics and defect population prevent this from occurring. The ratio of the theoretical lattice parameters for BCC (2.83 Å), L2₁ (5.70 Å), and G-phase (11.17 Å) are roughly equal to 1:2:4, and their structures are cubic, suggesting minimal strains associated with the coherency between these phases, which agrees with the presented TEM results.

3.4 Precipitate evolution on the early stage of aging

Quantitative changes in the precipitate radius, volume fraction, number density and composition, as a function of the increased aging time, are plotted in **Figure 10a, b, c and d**, respectively. The 24 h-aging period appears to denote a general cutoff point for the evolution of precipitates. Aging at 560°C for longer time corresponded to a plateau in particle size, decrease in volume fraction for the Ti containing compositions and plateau in volume fraction for the Nb and Ta containing compositions, and decrease in number-density of all G-phase structures (**Figure 10b and c**).

The measured average radius of G-phase precipitates is found to be the largest in the 2Ta alloy, where it reaches ~7 nm, and changes in the descending order as Ni₁₆Ta₆Si₇ > Ni₁₆Nb₆Si₇ > Ni₁₆Ti₆Si₇ (**Figure 10a**). The volume fractions approach an equilibrium content of 2~3 vol. % for the Nb and Ti containing G-phases (**Figure 10b**). The precipitate number-density was high, ~10²³/m³, at 24 h-aging state with the exception of the Ni₁₆Ta₆Si₇ G-phase, and then it decreased with aging time up to 96 h in all alloys due to particle coarsening (**Figure 10c**). These results suggest that to achieve the highest number density and lowest precipitate size for G-phase strengthening purposes, it may be best to use Ti as a G-phase former.

There is only a marginal difference in particle compositions between the 24 h- and 96 h-aging conditions as shown in **Figure 10d**, which implies that all aged alloys have already reached equilibrium G-phase compositions at their early stage of aging (~24 h). APT measurements suggest that all G-phase compositions show a substantial

concentration of Fe. The $\text{Ni}_{16}\text{Ti}_6\text{Si}_7$ G-phase is measured to contain ~ 10 at.% (Fe) while the $\text{Ni}_{16}\text{Ta}_6\text{Si}_7$ and $\text{Ni}_{16}\text{Nb}_6\text{Si}_7$ possess as much as ~ 30 at.%. By matching the atomic ratios of Ni: Ti/Nb/Ta: Si and considering the total precipitate compositions, it could be deduced that Fe is most likely to occupy the Ni site. The APT results fall within the range of DFT predictions on the solubility limits (a method that has been used with success in the past for $\text{Ni}_{16}\text{Mn}_6\text{Si}_7$ [21, 30]).

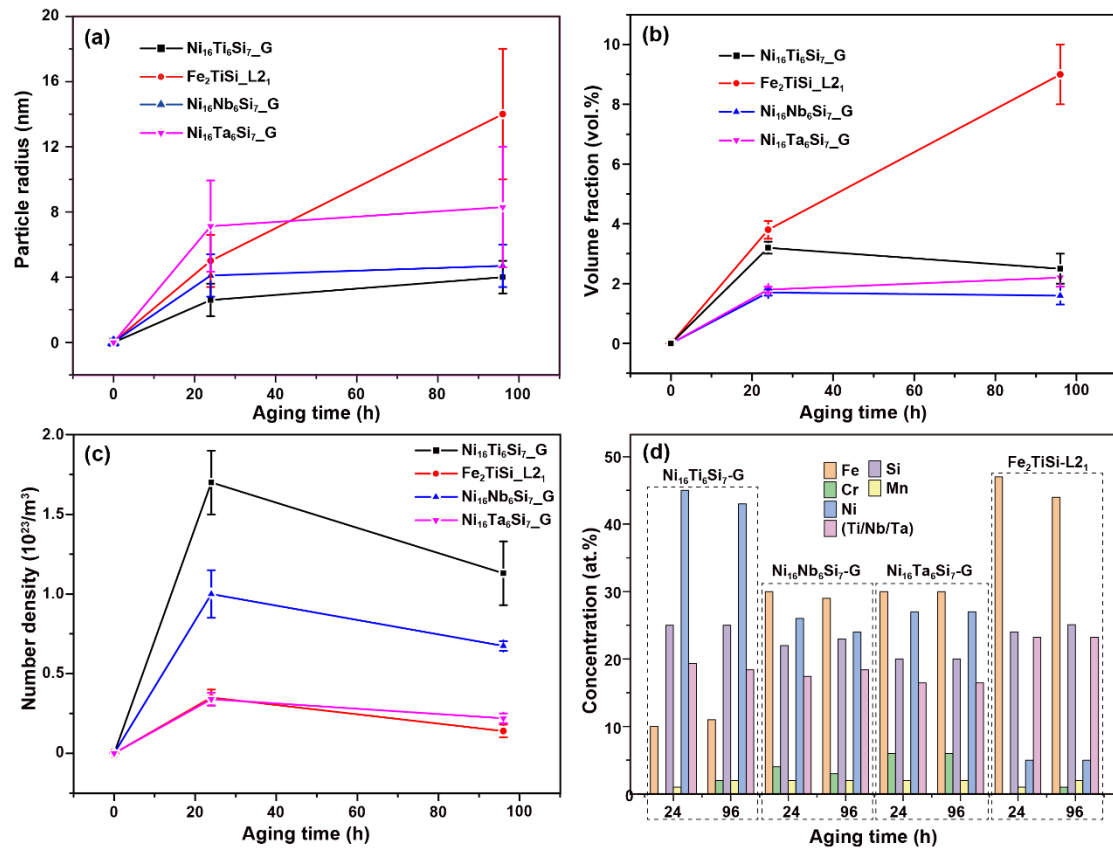


Figure 10. Quantitative precipitate (G and L₂₁ phase) statistics through APT characterization: (a) particle radii, (b) volume fractions, (c) particle number density, (d) chemical compositions.

4. Discussion

Considering the complexity of the microstructural evolution for 2Ti alloy during 560°C-aging, a qualitative schematic, based on the APT analysis and DFT calculations, was drawn and presented in **Figure 11**. At the early stages of aging (5 h), the $\text{Ni}_{16}\text{Ti}_6\text{Si}_7$ G-phase preferentially precipitates in an intragranular manner within ferrite grains, which is consistent with the strong age-hardening effect observed for the 2Ti alloy in our previous work [22]. When the Ni, Ti and Si migrate and cluster, the flux of Fe and Cr proceeds in the opposite direction, the Fe-, Ti- and Si-rich concentration gradient around G-phase particles appears to be formed simultaneously, which provided the compositional fluctuation condition for subsequent precipitation of the $\text{Fe}_2\text{TiSi-L2}_1$ phase. As the aging time increases, the $\text{Fe}_2\text{TiSi-L2}_1$ phase starts to nucleate on the surface of the $\text{Ni}_{16}\text{Ti}_6\text{Si}_7$ G-phase particle and finally grows around it to form a G/ L2_1 -envelope heterostructure. As the 2Ti alloy was further aged, these G/ L2_1 -envelope particles start to compete with each other for growth and coarsening. It could be deduced that the growth of L2_1 phase at the expense of the G-phase may occur due to the combination of kinetic and thermodynamic factors, e.g. G-phase nucleates faster, but L2_1 is more stable and “pulls” Ti out of the G-phase during growth. The heterogeneous nature of the nucleation may arise due to the interfacial energy differences between the different planes of G-phase and L2_1 i.e. it is likely the cube-on-cube orientations are more energetically favorable than other facets given the integer multiplicity of the lattice parameters of the BCC, L2_1 and G-phase.

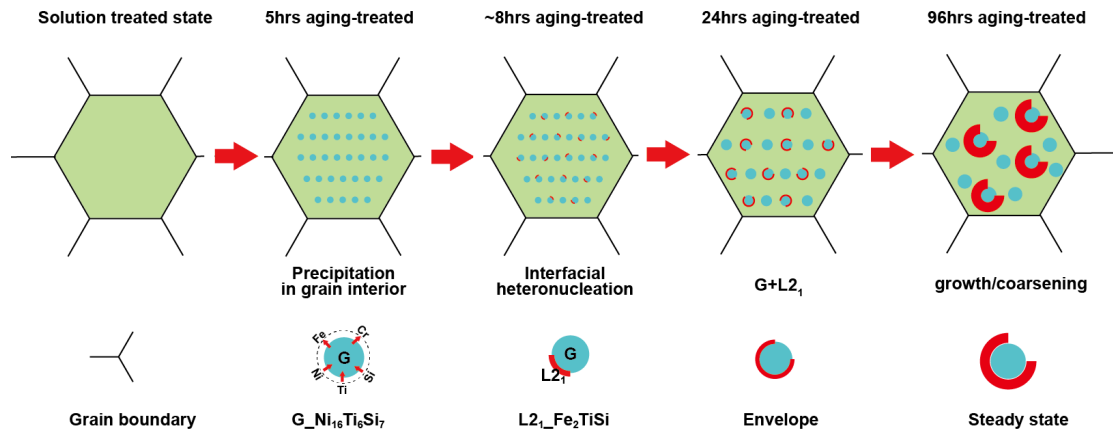


Figure 11. Schematic of microstructural evolution of the 2Ti alloy during aging at 560°C.

The 2Nb and 2Ta alloys have a much simpler precipitate evolution. Both the $\text{Ni}_{16}\text{Nb}_6\text{Si}_7$ and $\text{Ni}_{16}\text{Ta}_6\text{Si}_7$ G-phases nucleate intragranularly within the ferritic grains interiors, and then go through the process of growth and coarsening without secondary precipitation (**Figures 6 and 7**). The 2Mn alloy has not been included in the above discussion due to the prolonged incubation period (60~90 days) of the $\text{Ni}_{16}\text{Mn}_6\text{Si}_7$ G-phase. The square-like morphology (**Figure 2h**) of the $\text{Ni}_{16}\text{Mn}_6\text{Si}_7$ G-phase and their arrangement characteristic that align with each other strongly imply they are coherent with the ferritic matrix. Considering the minimization of the elastic modulus difference between precipitate and matrix, the $\text{Ni}_{16}\text{Mn}_6\text{Si}_7$ G-phase could be the best phase to avoid strain localization effects during plastic deformation. However, more research is needed to find a way to accelerate its precipitation.

5. Conclusions

In this work, the precipitation behavior of four novel alloys of nominal composition of Fe-20Cr-3Ni-3Si-X (X=2Mn, 1Mn-2Ti, 1Mn-2Nb and 1Mn-2Ta) (wt.%) were studied. The $\text{Ni}_{16}\text{M}_6\text{Si}_7$ G-phase precipitated quickly at ≤ 24 h when M = Nb, Ta and Ti. However, the $\text{Ni}_{16}\text{Mn}_6\text{Si}_7$ G-phase did not precipitate after 90 days, unless additional cold rolling was performed prior to aging between 400-500°C. Contributing factors to this sluggish precipitation for the 2Mn alloy were the small difference in the magnitude of enthalpy of formation between the $\text{Ni}_{16}\text{Mn}_6\text{Si}_7$ G-phase and the BCC phase and the lower solubility of Fe in the G-phase, with respect to the cases where M = Nb, Ta or Ti.

For the cases where M = Nb, Ta and Ti, the G-phases precipitated uniformly in the ferrite matrix. The aging of M = Nb and Ta alloys yielded a similar increase in microhardness of ~ 100 HV. However, for M = Ti the microhardness increase was measured to be ~ 275 HV. This increased hardening is attributed to the formation of the $\text{Ni}_{16}\text{Ti}_6\text{Si}_7$ G-phase and $\text{Fe}_2\text{TiSi-L2}_1$ Heusler phase. APT and TEM analyses determined that the Heusler phase nucleated heterogeneously on the G-phase and formed an envelope structure around the $\text{Ni}_{16}\text{Ti}_6\text{Si}_7$ G-phase cores. DFT results determined that the $\text{Fe}_2\text{TiSi-L2}_1$ phase is energetically favorable for Ni-lean chemistries.

Acknowledgements

This work was financially funded by the National Natural Science Foundation of China (Grant No. 51971082) and the National Post-doctoral Program for Innovative Talents (Grant No. BX20200103). APT research conducted by Junhua Luan and Zengbao Jiao at the Inter-University 3D Atom Probe Tomography Unit of City University of Hong Kong were supported by the CityU grant 9360161 and NSFC grant 51801169. TEM characterization conducted by Yuren Wen was funded by “the Fundamental Research Funds for the Central Universities” (No. 06500099). Mark Wenman and Daniel King were funded by EPSRC (Grant No. EP/P005101/1). The DFT calculations were undertaken with the assistance of resources provided by Tier 2 EPSRC resource allocation on Cambridge computing facilities (CSD3).

Conflicts of interest

The authors declare they have no conflicts of interest.

Reference

- [1] A. Grytsiv, X.-Q. Chen, P. Rogl, R. Podloucky, H. Schmidt, G. Giester, V. Pomjakushin, Crystal chemistry of the G-phases in the {Ti, Zr, Hf}-Ni-Si systems, *J. Solid State Chem.* 180(2) (2007) 733-741.
- [2] X. Yan, A. Grytsiv, P. Rogl, V. Pomjakushin, X. Xue, On the crystal structure of the Mn-Ni-Si G-phase, *J. Alloy. Compd.* 469(1) (2009) 152-155.
- [3] B. Zhang, F. Xue, S.L. Li, X.T. Wang, N.N. Liang, Y.H. Zhao, G. Sha, Non-uniform phase separation in ferrite of a duplex stainless steel, *Acta Mater.* 140 (2017) 388-397.
- [4] A. Mateo, L. Llanes, M. Anglada, A. Redjaimia, G. Metauer, Characterization of the intermetallic G-phase in an AISI 329 duplex stainless steel, *J. Mater. Sci.* 32 (17) (1997) 4533-4540.
- [5] C. Pareige, S. Novy, S. SAILLET, P. Pareige, Study of phase transformation and mechanical properties evolution of duplex stainless steels after long term thermal ageing (>20 years), *J. Nucl. Mater.* 411(1) (2011) 90-96.
- [6] C. Pareige, J. Emo, S. SAILLET, C. Domain, P. Pareige, Kinetics of G-phase precipitation and spinodal decomposition in very long aged ferrite of a Mo-free duplex stainless steel, *J. Nucl. Mater.* 465 (2015) 383-389.

- [7] I. Shuro, H.H. Kuo, T. Sasaki, K. Hono, Y. Todaka, M. Umemoto, G-phase precipitation in austenitic stainless steel deformed by high pressure torsion, *Mat. Sci. Eng. A* 552 (2012) 194-198.
- [8] Y. Matsukawa, T. Takeuchi, Y. Kakubo, T. Suzudo, H. Watanabe, H. Abe, T. Toyama, Y. Nagai, The two-step nucleation of G-phase in ferrite, *Acta Mater.* 116 (2016) 104-113.
- [9] W.-Y. Chen, M. Li, X. Zhang, M.A. Kirk, P.M. Baldo, T. Lian, In situ TEM study of G-phase precipitates under heavy ion irradiation in CF8 cast austenitic stainless steel, *J. Nucl. Mater.* 464 (2015) 185-192.
- [10] H.J. Beattie, F.L. Versnyder, A New Complex Phase in a High-Temperature Alloy, *Nature* 178(4526) (1956) 208-209.
- [11] R.C. Ecob, R.C. Lobb, V.L. Kohler, The formation of G-phase in 20/25 Nb stainless steel AGR fuel cladding alloy and its effect on creep properties *J. Mater. Sci.* 22(8) (1987) 2867-2880.
- [12] H. Purzyńska, G. Golański, A. Zieliński, J.D. Dobrzański, M. Sroka, Precipitation study in Ti-stabilised austenitic stainless steel after 207,000 h of service, *Mater. High Temp.* 36(4) (2019) 296-303.
- [13] N. Vaché, P. Steyer, C. Duret-Thual, M. Perez, T. Douillard, E. Rauch, M. Véron, G. Renou, F. Dupouiron, C. Augustin, S. Cazottes, Microstructural study of the NbC to G-phase transformation in HP-Nb alloys, *Materialia* 9 (2020) 100593.
- [14] D. Wen, B. Jiang, Q. Wang, F. Yu, X. Li, R. Tang, R. Zhang, G. Chen, C. Dong, Influences of Mo/Zr minor-alloying on the phase precipitation behavior in modified 310S austenitic stainless steels at high temperatures, *Mater. Des.* 128 (2017) 34-46.
- [15] S. Li, Y. Wang, X. Wang, F. Xue, G-phase precipitation in duplex stainless steels after long-term thermal aging: A high-resolution transmission electron microscopy study, *J. Nucl. Mater.* 452(1) (2014) 382-388.
- [16] T. Hamaoka, A. Nomoto, K. Nishida, K. Dohi, N. Soneda, Accurate determination of the number density of G-phase precipitates in thermally aged duplex stainless steel, *Philos. Mag.* 92(22) (2012) 2716-2732.
- [17] A.S. Schulz-Beeker, H.P. Hougardy, Development of High-Strength Martensite by Age-Hardening of Coherent Intermetallic Precipitates, *European Symposium on Martensitic Transformations* (1989) 473-480.
- [18] A. Gemperle, J. Gemperlová, W. Sha, G.D.W. Smith, Aging behaviour of cobalt free chromium containing maraging steels, *Mater. Sci. Tech.* 8(6) (1992) 546-554.
- [19] P. Staron, B. Jamnig, H. Leitner, R. Ebner, H. Clemens, Small-angle neutron scattering analysis of the precipitation behaviour in a maraging steel, *J. Appl. Crystallogr.* 36(3 Part 1) (2003) 415-419.

- [20] W.W. Sun, R.K.W. Marceau, M.J. Styles, D. Barbier, C.R. Hutchinson, G phase precipitation and strengthening in ultra-high strength ferritic steels: Towards lean ‘maraging’ metallurgy, *Acta Mater.* 130 (2017) 28-46.
- [21] D.J.M. King, M. Yang, T.M. Whiting, X. Liu, M.R. Wenman, G-phase strengthened iron alloys by design, *Acta Mater.* 183 (2020) 350-361.
- [22] M. Yang, J. Zhu, T. Yang, J. Luan, Z. Jiao, X. Fan, B. Kuhn, X. Xiong, C. Wang, C.T. Liu, X. Liu, A novel ferritic steel family hardened by intermetallic compound G-phase, *Mat. Sci. Eng. A* 745 (2019) 390-399.
- [23] M. Yang, J. Zhu, C. Wu, S. Yang, Z. Shi, C. Wang, X. Liu, Microstructural evolution and precipitation strengthening in a new 20Cr ferritic trial steel, *Mat. Sci. Eng. A* 742 (2019) 734-742.
- [24] M. Yang, C. Wang, S. Yang, Z. Shi, X. Liu, New insights into the precipitation strengthening of ferritic steels: Nanoscale G-phase particle, *Mater. Lett.* 209 (2017) 134-137.
- [25] M.K. Miller, K.F. Russell, Atom probe specimen preparation with a dual beam SEM/FIB miller, *Ultramicroscopy* 107(9) (2007) 761-766.
- [26] G. Kresse, J. Furthmüller, Software VASP, vienna (1999), *Phys. Rev. B* 54(11) (1996) 169.
- [27] G. Kresse, D. Joubert, From ultrasoft pseudopotentials to the projector augmented-wave method, *Phys. Rev. B* 59(3) (1999) 1758.
- [28] M. Methfessel, A. Paxton, High-precision sampling for Brillouin-zone integration in metals, *Phys. Rev. B* 40(6) (1989) 3616.
- [29] J.P. Perdew, K. Burke, M. Ernzerhof, Generalized gradient approximation made simple, *Phys. Rev. Lett.* 77(18) (1996) 3865.
- [30] D.J.M. King, P.A. Burr, S.C. Middleburgh, T.M. Whiting, M.G. Burke, M.R. Wenman, The formation and structure of Fe-Mn-Ni-Si solute clusters and G-phase precipitates in steels, *J. Nucl. Mater.* 505 (2018) 1-6.
- [31] D. King, P. Burr, S. Middleburgh, T. Whiting, M. Burke, M. Wenman, The formation and structure of Fe-Mn-Ni-Si solute clusters and G-phase precipitates in steels, *J. Nucl. Mater.* 505 (2018) 1-6.
- [32] G.R. Odette, Radiation induced microstructural evolution in reactor pressure vessel steels, Materials Research Society, United States, 1995.
- [33] H. Ke, P. Wells, P.D. Edmondson, N. Almirall, L. Barnard, G.R. Odette, D. Morgan, Thermodynamic and kinetic modeling of Mn-Ni-Si precipitates in low-Cu reactor pressure vessel steels, *Acta Mater.* 138 (2017) 10-26.
- [34] N. Almirall, P.B. Wells, H. Ke, P. Edmondson, D. Morgan, T. Yamamoto, G.R. Odette, On the Elevated Temperature Thermal Stability of Nanoscale Mn-Ni-Si Precipitates Formed at Lower Temperature in Highly Irradiated Reactor Pressure

- Vessel Steels, *Sci. Rep.* 9(1) (2019) 9587.
- [35] W. Xiong, H. Ke, R. Krishnamurthy, P. Wells, L. Barnard, G.R. Odette, D. Morgan, Thermodynamic models of low-temperature Mn-Ni-Si precipitation in reactor pressure vessel steels, *MRS Commun.* 4(3) (2014) 101-105.
- [36] D. King, S. Middleburgh, P. Burr, T. Whiting, P. Fossati, M. Wenman, Density functional theory study of the magnetic moment of solute Mn in bcc Fe, *Phys. Rev. B* 98(2) (2018) 024418.
- [37] N. Kourov, V. Marchenkov, A. Korolev, L. Stashkova, S. Emel'yanova, H. Weber, Specific features of the properties of half-metallic ferromagnetic Heusler alloys Fe_2MnAl , Fe_2MnSi , and Co_2MnAl , *Phys. Solid State* 57(4) (2015) 700-708.
- [38] L. Chen, Z. Li, L. Liu, N. Sekimura, N. Soneda, Study of the effect of Ni on solute clustering in α -Fe, *Nucl. Instrum. Meth. B* 453 (2019) 28-31.
- [39] P.D. Styman, J.M. Hyde, A. Morley, K. Wilford, N. Riddle, G.D. Smith, The effect of Ni on the microstructural evolution of high Cu reactor pressure vessel steel welds after thermal ageing for up to 100,000 h, *Mat. Sci. Eng. A* 736 (2018) 111-119.
- [40] L. T. Belkacemi, E. Meslin, B. Decamps, B. Radiguet, J. Henry, Radiation induced bcc-fcc phase transformation in a Fe3%Ni alloy, *Acta Mater.* 161 (2018) 61-72.
- [41] M. K. Miller, K. F. Russell, Embrittlement of RPV steels: An atom probe tomography perspective, *J. Nucl. Mater.* 371 (1-3) (2007) 145-160.